Solar Physics (2005) 226: 97–119 © Springer 2005

$2\frac{1}{2}$-DIMENSIONAL RECONNECTION MODEL AND ENERGY RELEASE IN SOLAR FLARES

BOJAN VRŠNAK[1] and MARINA SKENDER[2]
[1]*Hvar Observatory, Faculty of Geodesy, Kačićeva 26, HR-10000 Zagreb, Croatia*
(e-mail: bvrsnak@geodet.geof.hr)
[2]*Rudjer Bošković Institute, Bijenička 54, HR-10001 Zagreb, Croatia*
(e-mail: marina@rudjer.irb.hr)

(Received 18 May 2004; accepted 8 August 2004)

Abstract. We employ a $2\frac{1}{2}$-dimensional reconnection model to analyse different aspects of the energy release in two-ribbon flares. In particular, we investigate in which way the systematic change of inflow region variables, associated with the vertical elongation of current sheet, affects the flare evolution. It is assumed that as the transversal magnetic field decreases, the ambient plasma-to-magnetic pressure ratio increases, and the reconnection rate diminishes. As the transversal field decreases due to the arcade stretching, the energy release enhances and the temperature rises. Furthermore, the magnetosonic Mach number of the reconnection outflow increases, providing the formation of fast mode standing shocks above the flare loops and below the erupting flux rope. Eventually, in the limit of a very small transversal field the reconnection becomes turbulent due to a highly non-linear response of the system to small fluctuations of the transversal field. The turbulence results in the energy release fragmentation which increases the release efficiency, and is likely to be responsible for the impulsive phase of the flare. On the other hand, as the current sheet stretches to larger heights, the ambient plasma-to-magnetic pressure ratio increases which causes a gradual decrease of the reconnection rate, energy release rate, and temperature in the late phase of flare. The described magnetohydrodynamical changes affect also the electron distribution function in space and time. At large reconnection rates (impulsive phase of the flare) the ratio of the inflow-to-outflow magnetic field strength is much smaller than at lower reconnection rates (late phase of the flare), i.e., the corresponding loss-cone angle becomes narrower. Consequently, in the impulsive phase a larger fraction of energized electrons can escape from the current sheet downwards to the chromosphere and upwards into the corona – the dominant flare features are the foot-point hard X-ray sources and type III radio bursts. On the other hand, at low reconnection rates, more particles stay trapped in the outflow region, and the thermal conduction flux becomes strongly reduced. As a result, a superhot loop-top, and above-the-loop plasma appears, as sometimes observed, to be a dominant feature of the gradual phase.

1. Introduction

Soft X-ray observations reveal that during solar flares the magnetic field topology changes from an initially intricate, clearly non-potential configuration, to a relaxed, nearly potential system of post-flare loops (e.g., Sakurai, 1993; Aurass *et al.*, 1999). So, the field lines connect different foot-points before and after the flare, implying that they have to reconnect in the course of flare. Consequently, the flare is considered to be a result of a reconnection-associated release of free energy contained in the initial configuration.

The powerful energy release such as observed in flares requires a sufficiently fast-reconnection process. An important step in finding the appropriate physical mechanism was accomplished by Furth, Kileen, and Rosenbluth (1963), who realized that a long current sheet becomes unstable to the tearing instability. Such a process was subsequently identified in laboratory plasma experiments (e.g., Irby, Drake, and Griem, 1979), which were soon applied also to the solar flare research (e.g., Bulanov, Dogel, and Frank, 1984; Brown *et al*., 2002).

According to the fast-reconnection model proposed by Petschek (1964), the reconnection itself takes place within a tiny diffusion region (DR) which is thin enough to provide the balance of the magnetic flux inflow and the magnetic field diffusion. On the other hand, the DR must be also short enough to provide the balance of the plasma inflow and outflow even at the high reconnection rates required for a powerful energy release.

Furthermore, Petschek (1964) predicted a bifurcation of the current sheet into two pairs of standing slow-mode shocks (SMSs). Such shocks have been identified in numerical simulations (e.g., Sato and Hayashi, 1979), and in the Earth's magnetotail (e.g., Feldman *et al*., 1984, 1985; Smith *et al*., 1984). There is also some evidence which suggests they may occur in laboratory experiments (Stenzel and Gekelman, 1979, but see also Shay *et al*. 1998, 2001) and solar flares (Tsuneta, 1996).

The fast-reconnection mechanism is fruitfully incorporated into the two-ribbon flare models. The two-ribbon flare occurs during the eruption of a sheared magnetic field arcade, which may (e.g., Low, 2001) or may not (e.g., Antiochos, DeVore, and Klimchuk, 1999) contain a flux rope. After the arcade lift-off, a current sheet is created below a flux rope (see right panel of Figure 1) even if a flux rope was not present initially (Martens and Kuin, 1989; Lin and Forbes, 2000; Lin, 2004). As the flux rope rises, the current sheet elongates, and when its length-to-width ratio becomes large enough, the tearing instability sets in (see, e.g., Furth, Kileen, and Rosenbluth (1963), Ugai (1987), Gekelman and Pfister (1988), and Vršnak *et al*. (2003), for the analytical, numerical, experimental, and observational results, respectively).

Reconnection in two-ribbon flares has been extensively studied using numerical MHD. The studies successively included effects of the photospheric line tying (Forbes and Priest, 1982), change of the DR height (Forbes, 1986), different plasma-to-magnetic pressure ratio (Magara *et al*., 1996; Yokoyama and Shibata, 2001), radiation (Forbes and Malherbe, 1991), thermal conduction (Yokoyama and Shibata, 1997, 2001), anomalous resistivity (Ugai, 1992; Yokoyama and Shibata, 2001), the effects of chromospheric "evaporation" (Yokoyama and Shibata, 2001), the presence of the transversal field (Cheng *et al*., 2003), etc.

On the other hand, analytical studies mainly consider the conditions in the current sheet itself (e.g., Somov and Titov, 1985; Somov, 1986; Litvinenko and Somov, 1993; Somov and Kosugi, 1997; Craig and Litvinenko, 2002; Litvinenko, 2003, etc.), only occasionally addressing the evolutionary aspect (e.g., Martens and Kuin, 1989; Vršnak *et al*., 1989; Lin and Forbes, 2000; Lin, 2004), or the actual

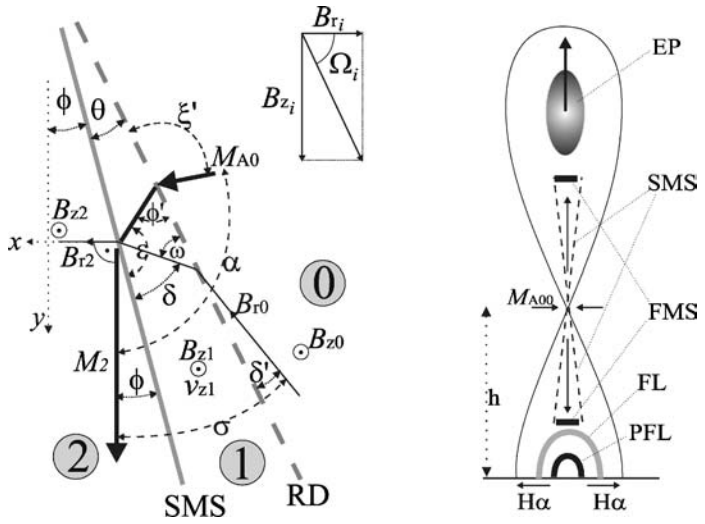

Figure 1. Left: The reconnection model (only one quadrant shown). Flows (*bold-black arrows*), magnetic field (*thin-black arrows*), and discontinuities (SMS – slow-mode shock; RD – rotational discontinuity), are shown together with the definition of angles and various vector components. Note that ϕ, θ, and δ' are oversized. *Right:* The reconnection model incorporated into a two-ribbon flare configuration; EP – eruptive prominence, Hα – chromospheric flare ribbons, FL – hot flare loops, PFL – post-flare loops. The plasma inflows are directed in the horizontal $\pm x$-direction (M_{A00}) and the outflows are in the vertical $\pm y$-direction. The photospheric magnetic inversion line lies in the horizontal z-direction. The magnetic X-line is aligned with the z-axis at the height h.

two-ribbon flare topology (Tsuneta, 1996; Tsuneta and Naito, 1998; Somov and Kosugi, 1997).

In this paper, we investigate and systemize some aspects of the $2\frac{1}{2}$-dimensional ($2\frac{1}{2}$-D)[1] reconnection problem, which might be relevant for comprehending the onset and development of solar flares. The analysis is based on the $2\frac{1}{2}$-D extension of the Petschek's model (Petschek and Thorne, 1967; Soward, 1982). In particular, we use analytical solutions based on the jump relations at the current sheet previously obtained by Skender, Vršnak, and Martinis (2003), to infer in which way the change of inflow region parameters affects the energy release in the flare. We apply the results primarily to two-ribbon flares since they can be represented well by a $2\frac{1}{2}$-D model. Furthermore, flares of this type are usually large, providing spatially resolved measurements of plasma parameters (e.g., Tsuneta, 1996; Uchida *et al.*, 2001; Sui and Holman, 2003; Kundu *et al.*, 2004), as well as an insight into plasma flows and changes of the coronal magnetic field configuration (e.g., Yokoyama *et al.*, 2001; Innes, McKenzie, and Wang, 2003; Vršnak *et al.*, 2003; Wang *et al.*, 2003; Chen *et al.*, 2004).

[1] 2-D model means that the magnetic field and plasma flow have only two (coplanar) components and that all quantities are invariant in the third direction. In $2\frac{1}{2}$-D models, the third component of the magnetic field and flow is allowed, but all quantities are still invariant in the third direction.

In Section 2 we first briefly describe the reconnection model used by Skender, Vršnak, and Martinis (2003) and place it into an idealized two-ribbon flare ambience, to link the model quantities with the flare parameters. The model results relevant for the flare process are shown in Sections 3 and 4. The expressions used in evaluating the presented results are displayed later in Appendix A. In addition, in Appendix B we present the approximate solution by Soward (1982). The implications of our results are discussed in Section 5.

2. The Reconnection Model and Two-Ribbon Flares

According to the $2\frac{1}{2}$-D extension of Petschek's model, a rotational discontinuity (RD) forms upstream of the SMS (Petschek and Thorne, 1967; Soward, 1982). Furthermore, under conditions appropriate for solar flares, the reconnection outflow is supermagnetosonic (e.g., Forbes, 1986; Forbes and Malherbe, 1986) and a standing fast-mode shock (FMS) is formed at the location where the jet encounters an obstacle (Aurass, Vršnak, and Mann, 2002; Aurass, 2004). This is depicted in Figure 1-right, where one FMS is sited above the flare loops and the other below the eruptive prominence. The quantities that characterize the inflow region upstream of the RD are denoted by the subscript "0", the intermediate region between the RD and the SMS by "1", the outflow region between the SMSs by "2", and the region downstream of the FMS by "3".

The coordinate system used in the analysis (Figure 1) has the y-axis aligned with the symmetry axis of the system (corresponding to the vertical direction in the corona), whereas the x-axis is oriented perpendicular to the current sheet (horizontal direction in the corona). The angle between the SMS and the y-axis is denoted by ϕ, whereas the RD is inclined to the SMS at the angle θ (Figure 1-left). The xy-plane components of vectors are denoted by the subscript "r".

It is assumed in the model that the plasma flows into the RD at the velocity v_0, having only the xy-plane component, $\vec{v}_{r0}$, which is inclined to the symmetry axis of the system at the angle α (Figure 1-left). The Alfvén Mach number is defined by $M_{A0} = v_0/v_{A0}$, where $v_{A0} = B_0/\sqrt{\mu\rho_0}$ is the Alfvén velocity in the inflow region. We define also the dimensionless reconnection rate, representing the Alfvén Mach number based on the v_{x0} component of the inflow velocity, and the B_{y0} component of the inflowing magnetic field, $M_{A00} = v_{x0}/v_{A0y}$, where $v_{A0y} = B_{y0}/\sqrt{\mu\rho_0}$. In the Petschek's regime it amounts to 1–10% of the Alfvén speed (cf., Priest, 1982).

In the employed (anti)symmetric model, the z-component of the flow velocity appears only in the intermediate region (Soward, 1982). Its inclination with respect to the xy-plane is depicted by the angle Ω_V, defined by $v_{z1}/v_{r1} = \tan\Omega_V$. In an analogous way, we describe the z-component of the magnetic field (transversal field), $B_{zi}/B_{ri} = \tan\Omega_i$ (Figure 1-left), where $i = 0, 1, 2$ denotes the inflow, intermediate, and the outflow region, respectively (Figure 1-left).

The coupled system of RD–SMS jump relations has been solved in an approximate form by Soward (1982).[2] Recently, the problem was solved in its complete form by Skender, Vršnak, and Martinis (2003) – the set of jump relations (see Section II.B in Skender, Vršnak, and Martinis, 2003) is transformed into a system of 17 equations containing 21 dimensionless quantities (see Section II.D in Skender, Vršnak, and Martinis, 2003). Four of these quantities describe the physical state of the inflow region, and represent the input parameters that determine the reconnection geometry, the energy release rate, and the outflow plasma parameters. These quantities are:

(i) the plasma-to-magnetic pressure ratio $\beta_0 = p_0/p_{m0}$, where $p_{m0} = B_0^2/2\mu$;
(ii) the ratio of the transversal and the xy-plane magnetic field components $B_{z0}/B_{r0} = \tan\Omega_0$;
(iii) the dimensionless reconnection rate $M_{A00} = v_{x0}/v_{A0y}$;
(iv) the incidence angle α of the inflow, $\alpha \equiv \angle(\vec{v}_0, \vec{y})$.

Each of these four parameters is expected to change in the course of a flare at least due to inhomogeneous coronal structure. However, in two-ribbon flares, beside such stochastic variations, the inflow parameters experience also a systematic evolution, as outlined in the following.

Since the pre-flare arcade is strongly sheared, there is a non-zero transversal magnetic field component, B_z, associated with the current sheet. If too strong, the B_z component prevents an efficient energy release (Nishikawa and Sakai, 1982; Soward, 1982; Forbes and Malherbe, 1986; Frank, Bogdanov, and Markov, 2002; Heitsch and Zweibel, 2003). However, as the erupting flux rope rises, the arcade field lines are stretched vertically, so B_z gradually diminishes. In other words, the rapid energy release characterizing the impulsive phase of a two-ribbon flare, can start only after the eruption attains a sufficient height at which B_z, i.e., the angle Ω_0, becomes sufficiently small. After the flare onset, Ω_0 continues to decrease due to the ongoing vertical stretching of the arcade, and it is reasonable to assume that at a given point it becomes $\Omega_0 \approx 0$.

Another relevant parameter which changes during the flare is the reconnection rate M_{A00}. This is indicated by decreasing expansion speed of flare ribbons (e.g., Wang *et al.*, 2003), and a slower late-phase growth of the loop system (e.g., Forbes and Acton, 1996).

As the current sheet elongates vertically, there are also considerable environmental changes which have to be taken into account. The magnetic field becomes weaker, the coronal density decreases, whereas the plasma-to-magnetic pressure ratio β_0 increases (Gary, 2001; Vršnak *et al.*, 2002). Furthermore, the effects of the

[2] Soward (1982) considered perpendicular inflow ($\alpha = 90^\circ$) of low Mach number ($M_{A00} \ll 1$). Furthermore, it was assumed that in the intermediate region the transversal magnetic field component B_z is much larger than the reconnection-plane component B_r. Hereinafter, we call that "Soward's approximation" (see Appendix B).

solar wind might become important, affecting the incidence angle α of the inflow (Cargill and Priest, 1982).

3. Outflow Jet

3.1. SMS-RELATED QUANTITIES

The basic physical characteristics of the outflow region, such as temperature, density, magnetic field strength, and flow velocity, are determined primarily by Ω_0 and β_0, whereas the effect of M_{A00} is generally very weak, resulting in deviations smaller than 1% (Skender, Vršnak, and Martinis, 2003). The influence of the inflow incidence angle α is somewhat more important, but only at large M_{A00} combined with substantial deviations from $\alpha = 90^\circ$. On the other hand, the basic geometrical properties, such as e.g., the inclination of the SMS, or the angle between the SMS and the RD, depend primarily on M_{A00} (see Appendix B).

Figures 2a and 2b show the density and temperature jumps at the SMS (n_2/n_1 and T_2/T_1, respectively) as a function of Ω_0 for different values of the ambient β_0. Note that differences caused by various M_{A00} cannot be resolved in Figure 2, demonstrating that Soward's approximation (see Appendix B) represents well the behaviour of n_2/n_1 and T_2/T_1. The magnetic field strength, density, and temperature do not change at the RD (Priest, 1982), i.e., $B_1 = B_0$, $T_1 = T_0$, and $n_1 = n_0$, implying also $\beta_1 = \beta_0$. Consequently, the temperature and density jumps at the SMS represent also the outflow values expressed relative to the ambient coronal conditions, since $n_2/n_1 = n_2/n_0$ and $T_2/T_1 = T_2/T_0$.

The bold lines, representing the outcome for $\beta_0 = 0.01$ and 0.1, depict roughly the limits of the flare conditions. The former value gives $(T_2/T_1)_{\max} \approx 40$, and the latter one $(T_2/T_1)_{\max} \approx 5$. Adopting for the coronal temperature, $T_0 \equiv T_1 = 1$–2 MK (Withbroe, 1988), it gives $T_2 = 40$–80 MK and $T_2 = 5$–10 MK, respectively. The former values are close to (or higher then) the upper limit of the observed temperatures (Uchida *et al.*, 2001; Aschwanden, 2002). On the other hand, an event characterized by temperatures below, e.g., 5 MK is usually not considered to be a flare. Actually, the values in the range $\beta_0 \approx 0.01$–0.1 are consistent with other estimates of β_0 in the active region corona (Gary, 2001; Vršnak *et al.*, 2002). Following the same argument, one also finds that the flare conditions (in the case of $\beta_0 \approx 0.01$) become fulfilled only if $\Omega_0 \lesssim 45^\circ$ ($\Omega_0 = 45^\circ$ represents the perpendicularly oriented inflowing fields). In the case of $\beta_0 = 0.1$, the inflowing fields have to be practically antiparallel ($\Omega_0 \approx 0$) in order to achieve a five-fold temperature increase.

In Figure 2c we show the plasma-to-magnetic pressure ratio in the outflow, β_2, as a function of Ω_0. The graph shows that the outflow is generally dominated by the plasma pressure. However, note that despite the condition $\beta_2 \gg 1$, the geometry

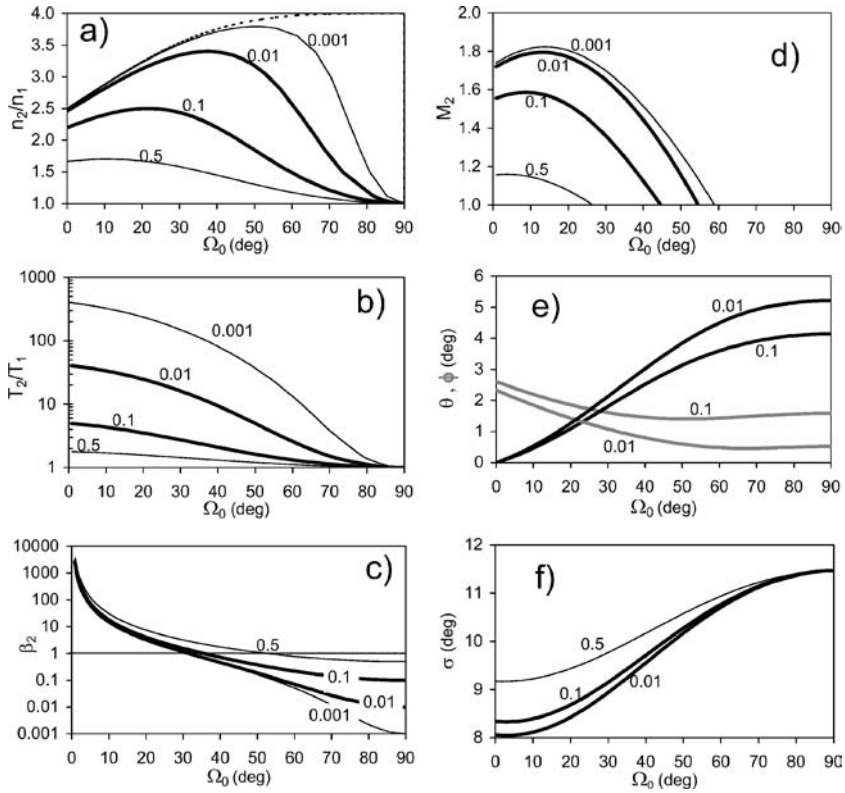

Figure 2. Conditions in the outflow jet shown for perpendicular inflow ($\alpha = 90^\circ$), and different values of β_0 (written at the curves): (a) density jump at the SMS – the *dashed line* represents the $\beta_0 = 0$ limit; (b) temperature jump; (c) plasma-to-magnetic pressure ratio in the outflow; (d) magnetosonic Mach number (only supermagnetosonic regime shown); (e) the angle between the SMS and the RD, θ (*black*), and the angle between the SMS and the y-axis, ϕ (*gray*), shown for $M_{A00} = 0.1$; (f) the angle between the xy-plane component of the inflowing magnetic field $\vec{B}_{r0}$ and the y-axis, shown for $M_{A00} = 0.1$.

and properties of the outflow are controlled magnetically due to the strong inflow field, where $\beta_1 = \beta_0 \ll 1$.

Unlike the temperature and density, the magnetosonic Mach number of the outflow, M_2, depends not only on Ω_0 and β_0, but also on the direction of the inflow (α), especially if the velocity component in the y-direction, v_{y0}, is large (caused by, e.g., solar wind or evaporation flow; see Cargill and Priest, 1982). In Figure 2d, the dependence $M_2(\Omega_0)$ is shown for $\alpha = 90^\circ$, whereas the dependence on α is presented later, in Figure 3. Figure 2d shows that the function $M_2(\Omega_0)$ peaks between $\Omega_0 \approx 10$ and 20°, depending on β_0, and that M_2 is smaller at larger β_0.

Figures 2e and 2f expose the behaviour of parameters which depict the basic geometry of the reconnection system. The angle ϕ defines the inclination of the SMS with respect to the y-axis, whereas θ represents the angle between the SMS and the

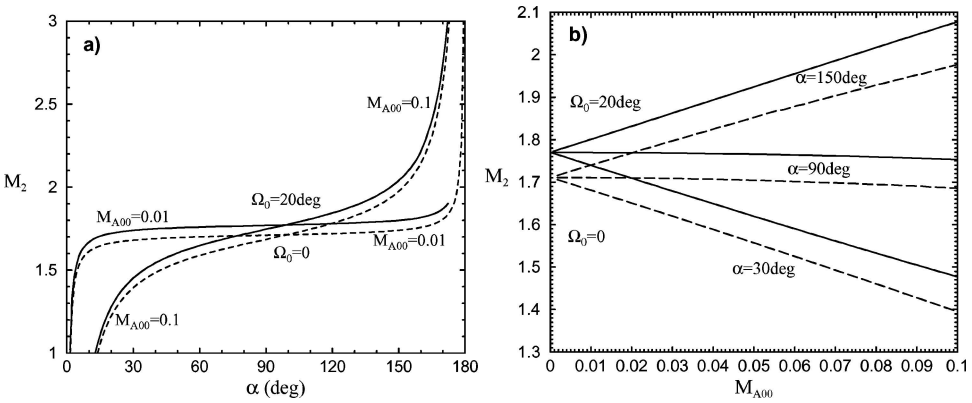

Figure 3. Magnetosonic Mach number of the outflow presented as a function of: (a) the incidence angle α for $M_{A00} = 0.01$ (*thin*) and 0.1 (*bold*), at $\Omega_0 = 0$ (*dashed*) and 20° (*full*); (b) the reconnection rate M_{A00} for $\alpha = 30$, 90, and 150°, at $\Omega_0 = 0$ (*dashed*) and 20° (*full*).

RD (Figure 1). The angle σ represents the inclination of the xy-plane component of the inflowing magnetic field $\vec{B}_{r0}$ with respect to the y-axis. The angle between $\vec{B}_{r0}$ and RD, δ', does not depend on Ω_0 (see Appendix B; the deviations from Soward's approximation are negligible). We show the results only for $M_{A00} = 0.1$, since all of these angles are basically proportional to M_{A00} (Appendix B). In the transition $\Omega_0 \to 0$, the RD and the SMS merge, i.e., $\theta \to 0$.

Figure 3 illustrates in which way the outflow Mach number M_2 depends on the incidence angle α and the reconnection rate.[3] The results are shown for $\Omega_0 = 0$ and 20°, at $\beta_0 = 0.01$. In Figure 3a, M_2 is shown as a function of the incidence angle α, for two values of the reconnection rate, $M_{A00} = 0.01$ and 0.1. The perpendicular inflow means $\alpha = 90°$, whereas $\alpha > 90°$ represents an inflow inclined in the direction of the outflow. The graph shows that the outflow Mach number is increased for $\alpha > 90°$, and decreased for $\alpha < 90°$, but the outcome is not a simple addition (subtraction) of the y-component of inflow velocity (note a slight asymmetry of the pattern with respect to $\alpha = 90°$). In Figure 3b we show the dependence of M_2 on the inflow velocity for three incidence angles ($\alpha = 150$, 90, and 30°).

In order to illustrate the role of the incidence angle α in the coronal environment, let us assume that the reconnection takes place at such heights where the solar wind is not negligible anymore. As an example, we take for the wind speed at the particular height $w = 50$ km s^{-1}, the ambient Alfvén velocity $v_A = 1000$ km s^{-1}, and the reconnection rate $M_{A00} = 0.1$. This means that the inflow velocity amounts to $|v_{x0}| = M_{A00} v_{A0} = 10$ km s^{-1}, implying that $\tan|\alpha| = |v_{x0}/v_{y0}| = |v_{x0}/w| = 10/50 = 0.2$, i.e., $|\alpha| = 11°$. The inflow is inclined upwards, and at such an angle one finds out (see Figure 3a) that the downward jet becomes submagnetosonic,

[3]The role of incidence angle was treated analytically also by Cargill and Priest (1982), but only for $\Omega_0 = 0$ (2-D case).

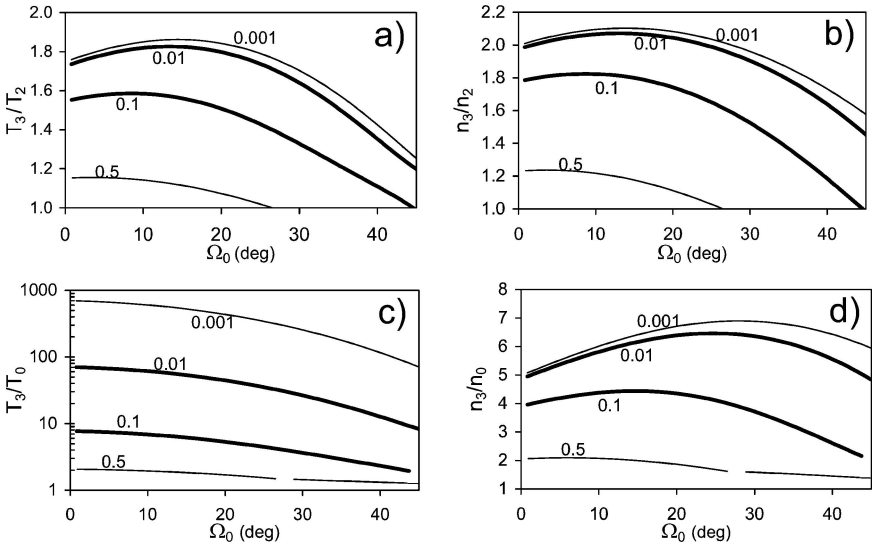

Figure 4. Characteristics of the FMS in the flare domain, shown for different values of β_0 (indicated by the curves), at $\alpha = 90^\circ$. (a and b) The temperature and density jumps at FMS. (c and d) The downstream FMS temperature and density normalized with respect to the inflow region values. The breaks in the $\beta_0 = 0.1$ and 0.5 curves depict the transition to the submagnetosonic regime.

whereas in the upward direction ($\alpha = 180^\circ - 11^\circ = 169^\circ$) the Mach number increases to $M_2 \approx 2.7$. Analogously, if the vortices behind the erupting flux rope (Cargill *et al*. 1996) create a downward flow component of, e.g., 50 km s^{-1} the plasma in the upward jet becomes submagnetosonic, whereas the downward one achieves $M_2 \approx 2.7$.

3.2. Formation and characteristics of the FMS

Figures 4a and 4b show the temperature and density jump at the FMS for the perpendicular inflow case, $\alpha = 90^\circ$. One finds out that in the flare-domain, the temperature is increased by a factor 1.6–1.8, and the density is increased by a factor of 1.8–2.1. These results are consistent with numerical simulations (e.g., Forbes, 1986; Yokoyama and Shibata, 2001). Note that the FMS is a perpendicular shock, so the jump of the magnetic field strength is equal to the density jump, $B_3/B_2 = n_3/n_2$ (Priest, 1982). The maximum amplitude of the FMS is achieved at $\Omega_0 \approx 10$–20°, when the outflow has the highest magnetosonic Mach number (Section 3.1).

According to Figure 3, at a large incidence angle and a large inflow speed M_{A00}, the outflow Mach number, and thus the FMS amplitude, can differ significantly from the values representing the perpendicular inflow. For example, in the $\alpha = 169^\circ$ case considered in Section 3.1, the FMS temperature and density jump amount to $T_3/T_2 = 3.2$ and $n_3/n_2 = 2.9$.

It should be emphasized that according to Figure 2c the FMS is basically a hydrodynamical shock ($\beta_2 \gg 1$), if only the flare domain is considered.

3.3. MAGNETIC MIRRORS AT SMS AND FMS

One of significant characteristics of the fast-reconnection geometry is a large difference of the magnetic field strength in the inflow and outflow region – the energy is released at the expense of the inflowing magnetic field, so the magnetic field strength in the outflow is much smaller than upstream of the SMS. The value of $B_1/B_2 \equiv B_{12}$ depends primarily on Ω_0 and M_{A00} (Figure 5a). The dependence on the plasma-to-magnetic pressure ratio β_0 is weak, which is demonstrated in Figure 5a,

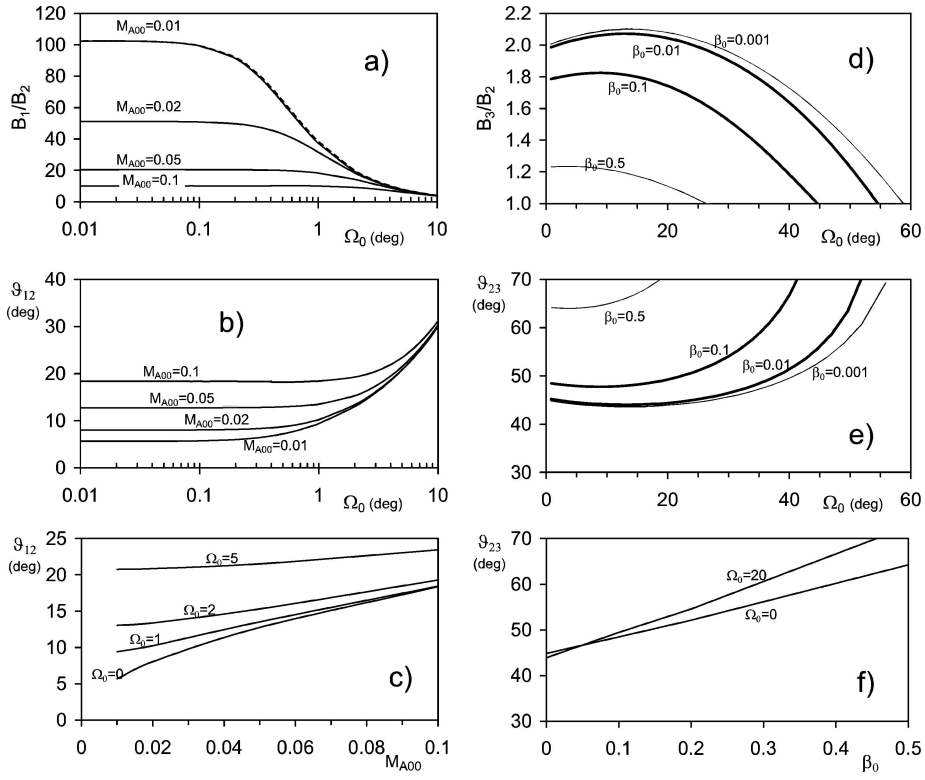

Figure 5. Magnetic mirrors at the SMS (left) and the FMS (right): (a) The jump of the magnetic field strength at the SMS presented as a function of Ω_0 for different reconnection rates M_{A00} at $\beta_0 = 0.01$ (the dashed line attached to the $M_{A00} = 0.01$ curve represents $\beta_0 = 0.1$). (b) The corresponding loss-cone angle ϑ_{12}. Note the logarithmic scale at the x-axis in (a) and (b). (c) The loss-cone angle presented as $\vartheta_{12}(M_{A00})$ for $\Omega_0 = 0$, 1, 2, and 5°. (d) The jump of the magnetic field strength at the FMS presented as a function of Ω_0 for different values of the inflow plasma-to-magnetic pressure ratio β_0, in the case of the perpendicular inflow, $\alpha = 90°$. (e) The corresponding loss-cone angle ϑ_{23}. (f) The loss-cone angle presented as $\vartheta_{23}(\beta_0)$ for $\Omega_0 = 0$ and 20°.

where the $B_{12}(\Omega_0)$ dependence at $M_{A00} = 0.01$ is shown for $\beta_0 = 0.01$ (full) and $\beta_0 = 0.1$ (dashed).

The background of the dependence $B_{12}(M_{A00})$ can be outlined considering the $\Omega_0 = 0$ case. A larger reconnection rate implies a larger angle between SMSs, 2ϕ, since $\phi \sim M_{A00}$ (see Appendix B). Consequently, the inflowing magnetic field lines also become more inclined, which implies that B_{12} decreases.

The behaviour of the corresponding magnetic mirror loss-cone angle, defined by $\sin^2 \vartheta_{12} = B_2/B_1$, is illustrated in Figures 5b and 5c. In the flare domain, the loss-cone angle ranges from very narrow $\vartheta_{12} \approx 5^\circ$, up to 40° (Figure 5b). The $\vartheta_{12}(\Omega_0)$ variation is larger at lower reconnection rates. At large Ω_0 the value of ϑ_{12} does not depend significantly on M_{A00}.

Although in the idealized model geometry the FMS is a perfect perpendicular shock, in reality the shock front (or magnetic field lines) is at least a bit curved (Somov and Kosugi, 1997; Tsuneta and Naito, 1998; Vršnak, 2004). So, the FMS can be treated as a quasi-perpendicular shock, and the loss-cone angle ϑ_{23} can be attributed to the magnetic field jump $B_{23} \equiv B_2/B_3$.

The magnetic field jump at the FMS generally depends on Ω_0 and β_0 (Figure 5d), reflecting the $M_2(\Omega_0, \beta_0)$ dependence illustrated previously in Figure 2d. However, inspecting the related change of ϑ_{23} (Figure 5e), one finds out that in the flare domain (e.g., $\Omega_0 < 45^\circ$ for $\beta_0 = 0.01$; see Section 3.1) the value of ϑ_{23} depends only weakly on Ω_0. A similar conclusion can be drawn if attention is paid in Figure 5f to the flare domain, $\beta_0 < 0.1$.

The loss-cone at the FMS is generally much broader than at the SMS ($\vartheta_{23} \gtrsim 45^\circ$). However, since M_2 depends on the inflow incidence angle α (Figure 3), the loss-cone width depends on α, too. Under favourable conditions (large α and M_{A00}), the loss-cone can become somewhat narrower. Considering the $\alpha = 169^\circ$ example presented in Section 3.1, one finds $\vartheta_{23} \approx 30-40^\circ$.

4. Intermediate Region

4.1. Geometrical changes in the transition $\Omega_0 \to 0$

Skender, Vršnak, and Martinis (2003) found that the geometry of the system changes very rapidly in the limit $\Omega_0 \to 0$. As shown therein, in the range $\Omega_0 \lesssim 1^\circ$ the transversal magnetic field component B_z in the intermediate region becomes comparable to, or smaller than the xy-plane component B_r, meaning that Soward's approximation is not valid anymore (see footnote "2" in Section 2.1).

In Figure 6 we show various geometrical parameters of the intermediate region, presented as a function of Ω_0 for $\alpha = 90^\circ$. The x-axis is displayed on a logarithmic scale to expose more transparently the changes at small Ω_0.

Figure 6a depicts in which way the angle between the plasma flow and the magnetic field, ζ, changes at $\Omega_0 \to 0$. If we trace the change from larger to smaller

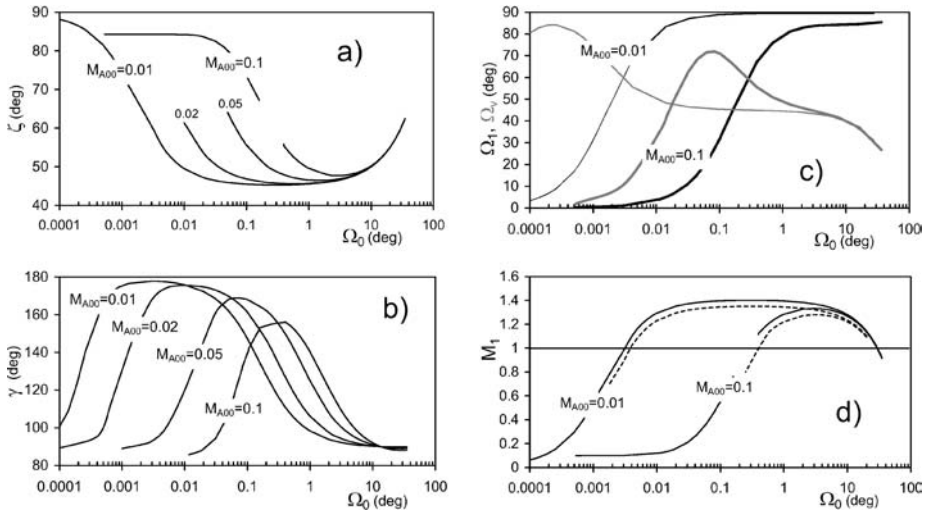

Figure 6. Change of various intermediate region quantities at $\Omega_0 \to 0$, shown for different reconnection rates M_{A00}. (a) The angle between the plasma flow and the magnetic field, ζ. (b) The same for the xy-plane components. (c) The inclination of the magnetic field from the xy-plane, Ω_1 (*black*) and the inclination of the flow, Ω_V (*gray*), shown for $M_{A00} = 0.01$ (*thin*) and $M_{A00} = 0.1$ (*thick*). (d) Magnetosonic Mach number M_1 of the intermediate region flow, shown for $\beta_0 = 0.01$ (*full*) and $\beta_0 = 0.1$ (*dashed*).

values of Ω_0, Figure 6a shows that ζ first gradually decreases to the minimum $\zeta_{\min} \approx 45^\circ$ and then sharply increases towards $\zeta \approx 90^\circ$ – the increase happens within a fraction of a degree.

Figure 6b outlines the change of the angle between the xy-plane components of the magnetic field and flow, $\gamma \equiv \angle(\vec{B}_{r1}, \vec{v}_{r1})$ (see Figure 1). In the transition $\Omega_0 \to 0$, the angle γ first increases from 90 to 180°, which is followed by a steep decrease back to 90°. At low reconnection rates, the entire change happens within $\Omega_0 \lesssim 1^\circ$ i.e., the change is very sharply peaked.

Figure 6c shows the associated change of the inclination of the intermediate region magnetic field, Ω_1 (black lines) and the plasma flow, Ω_V (gray lines). In the transition $\Omega_0 \to 0$, the transversal magnetic field exposes a sharp decrease ($\Omega_1 \to 0$) within $\Omega_0 \lesssim 1^\circ$. The flow direction shows a more complex behaviour before the transversal flow component eventually ceases ($\Omega_V \to 0$) at extremely small values of Ω_0.

The dependencies shown in Figures 6a – 6c do not depend on β_0 significantly – the difference between $\beta_0 = 0.1$ and $\beta_0 = 0.01$ cannot be resolved in the graph.

In a real situation, it is hardly possible that $\Omega_0 = 0$ is strictly satisfied. Certainly, fluctuations larger than $\Delta\Omega_0 = 1^\circ$ should be present along the current sheet. So, two neighbouring current sheet segments, although exposing only a slightly different Ω_0 in the inflow region, are characterized by a large difference in the field/flow

direction (up to 90°) in the intermediate region. The presence of such large field/flow distortions strongly implies that MHD turbulence sets in as $\Omega_0 \to 0$ (to be discussed in Section 5.3).

4.2. MACH NUMBER OF THE INTERMEDIATE REGION FLOW

Another potentially important characteristic of the intermediate region is depicted in Figure 6d. In the flare domain, there is an Ω_0 interval where the intermediate region flow becomes supermagnetosonic, $M_1 > 1$. Since in the transition $\Omega_0 \to 0$ the value of M_1 sharply decreases to the submagnetosonic regime, $M_1 < 1$, one can expect that the supermagnetosonic flow elements intermittently create shocks at locations where they meet submagnetosonic elements (the flow direction is also different for these elements, see Figure 6c). Note that shocks can be formed only if such a flow pattern persists for a time longer than needed for the shock completion (Vršnak and Lulić, 2000).

The magnetosonic Mach number M_1 and the associated shock amplitude depend on β_0 only weakly (Figure 6d), unlike the Mach number of the outflow jet, M_2 (Figure 2d). Inspecting in Figure 6a the field/flow angle ζ in the Ω_0 interval where $M_1 > 1$, one finds out that the supermagnetosonic flow creates an oblique fast-mode shock with the inclination of the magnetic field to the shock front of $\gtrsim 45°$. Finally, in contrast to the FMS formed in the outflow, where $\beta_2 \gg 1$, the intermediate region shock is created in the $\beta_1 \ll 1$ environment.

The regime of supermagnetosonic flows in the intermediate region partly overlaps with the $\Omega_0 \to 0$ stage, in particular the decrease to the $M_1 < 1$ regime at small Ω_0. Thus, the appearance of intermediate region shocks is closely associated with the transition into the turbulent reconnection state.

5. Implications

The evolutionary changes of the inflow region variables, described in the second part of Section 2, should be reflected in a systematic change of the flare plasma parameters. In the following, we discuss the implications of our results, paying attention primarily to the overall flare morphology and evolution.

5.1. THE TEMPERATURE

The hottest plasma, with temperatures two to three times higher than in the rest of the current sheet, should be located above the flare loops, downstream of the FMS. Indeed, very hot sources are sometimes resolved above the flare loops (e.g., Tsuneta, 1996; Uchida *et al.*, 2001; Petrosian, Donaghy, and McTiernan, 2002; Sui and Holman, 2003, and references therein). Since β_0 is generally larger at larger

heights, the temperature downstream of the FMS located at the base of the erupting flux rope should be lower than that above the flare loops.

Another interesting aspect regarding the influence of the plasma-to-magnetic pressure ratio, concerns the case when the arcade eruption and the associated reconnection process take place in a $\beta_0 > 0.1$ environment. According to Figure 2b, in such a case the outflow region plasma is not heated much, and the eruption should not be accompanied by a flare. Indeed, after coronal mass ejections that are associated with eruptions of quiescent filaments, a growing system of the so-called post-eruption loops is frequently observed in the EUV range. Such a loop system is morphologically quite similar to the flaring loop system, except for the fact that it is not hot enough to be seen in X-rays. The quiescent filament eruptions take place in quiet regions, where β is generally larger than in active regions (Wu *et al.*, 2001). So, it is reasonable to assume that the post-eruption loops appear as a result of the reconnection process analogous to that in two-ribbon flares. The primary difference being that they occur in a higher β environment. Moreover, quiescent filament eruptions generally start at relatively large heights (e.g., Feynman and Ruzmaikin, 2004), again being indicative of a larger-β ambience (Gary, 2001).

The dependence of the flare temperature on β_0 is indirectly indicated by some statistical scalings. For example, Ruždjak *et al*. (1989) have shown that on average the temperature in spotless flares is lower than in spot-group flares, consistent with larger values of β found in spotless regions (Wu *et al.*, 2001). The hottest flares are found to be those in which the Hα emission protrudes over major sunspot umbrae, indicating that the energy release takes place in very strong fields. Moreover, it was demonstrated by Vršnak *et al*. (1991) that in these flares the temperature is correlated with the magnetic field strength of the involved sunspot. Such a behaviour is consistent with the $T(\beta_0)$ dependence, since a stronger field implies a lower β.

5.2. THE DENSITY

The compression of plasma at both the SMS and the FMS has several important observational consequences. When radio-heliographic data are not available, the heights of radio sources are often estimated by assuming that the emission is excited at the local plasma frequency. Neglecting the effect of the enhanced density, and straightforward application of some coronal density model, leads to a significant underestimate of the source height. The plasma behind the FMS can be up to 10 times denser than in the ambient corona (see the $\alpha = 169^\circ$ example used in Sections 3.1 and 3.2), which corresponds to the factor around 3 in the emission frequency ($f \sim \sqrt{n}$). Taking, e.g., a source emitting at $f = 300$ MHz and applying the five-fold Saito (1970) coronal density model, being appropriate to describe the active region corona (Vršnak *et al.*, 2002), a nominal source height amounts to $h = 35$ Mm. However, taking into account the effect of the compression, one finds for the ambient plasma frequency $f^* \approx 100$ MHz, and the real height turns out to

be $h^* = 250$ Mm. Thus, the effect of the compression is sufficient to explain why radio sources of stationary type IV bursts, emitting at relatively high frequencies, are found at unexpectedly large heights (Vršnak *et al.*, 2003).

The next important aspect is the large density gradient at the SMS and the FMS. If the plasma radio emission is excited at these discontinuities, the emission is going to be broadband. For example, a pulsed electron beam passing across SMS would excite a radio pulse of relative bandwidth $\Delta f/f = \sqrt{n_2/n_0} - 1 \approx 0.6-0.9$. Furthermore, assuming that the entire current sheet excites radio waves at the local plasma frequency, and taking into account the overall density excess n_3/n_0 (see Figure 4d, and the $\alpha = 169^\circ$ example considered in Section 3.2), one finds that the corresponding relative bandwidth amounts to $(\Delta f/f)_{30} = 1$–2. Such a bandwidth is comparable with a typical type IV radio burst continuum: for example, for $\Delta f/f = 1.5$, one finds at $f = 200$ MHz a bandwidth of $\Delta f = 300$ MHz, i.e., the emission spans from 200 to 500 MHz.

On the other hand, if the plasma radio emission is excited at the FMS analogously as in the type II radio bursts (Aurass, Vršnak, and Mann, 2002: Vršnak *et al.*, 2002), it should appear as a non-drifting emission pattern split into two lanes, one excited in the upstream and the other in the downstream FMS region. The lanes should be separated by $\Delta f/f = \sqrt{n_3/n_2} - 1 = 0.1$–$0.2$, consistent with the "band-split" reported by Aurass, Vršnak, and Mann (2002). However, at a large incidence angle α, the band-split can become significantly larger – taking again the $\alpha = 169^\circ$ example, one finds $\Delta f/f \approx 0.7$. Furthermore, if the amplitudes of the two FMSs are affected by fluctuations of α caused by large scale vortices behind the moving flux rope, the variations of the amplitudes should be anti-correlated (see the example at the end of Section 3.1). A radio-emission signature of this kind was noticed by Aurass (2004).

5.3. MHD TURBULENCE

As shown in Section 4.1, in the transition $\Omega_0 \to 0$, the geometry of the system becomes extremely sensitive to small changes of Ω_0, which most likely leads to MHD turbulence. The reason why turbulence is expected to appear in the $\Omega_0 \to 0$ stage is found in the highly non-linear characteristics of the SMS/RD jump relations in this regime. If a small perturbation of Ω_0 is applied to an inflow region element, the flow and magnetic field in the corresponding intermediate region segment will have entirely different structures than in the adjacent elements (see Figure 6). Such a distortion inevitably perturbs the neighbouring segments, creating there conditions that do not match with the state of the corresponding inflow and outflow region elements.[4] So, these indirectly perturbed intermediate region segments have to respond by creating large-amplitude MHD waves which try to establish a new steady state by adjusting the inflow, outflow, and intermediate region parameters.

[4] A more detailed analysis shows that the intermediate region parameters can even attain values for which there is no steady-state solution at all.

However, this additionally perturbs the part of the inflow region where the initial disturbance was applied, as well as the elements farther out along the intermediate region. Due to the described feedback, it becomes impossible to create a new steady state, and turbulence eventually spreads across the whole current sheet. In such a state, many small-scale current sheets (X-points) and coalescing magnetic islands (O-points) are formed (Dmitruk *et al.*, 2003), presumably resulting in an avalanche type of energy release (e.g., Isliker, Anastasiadis, and Vlahos, 2001).

Since the perturbed layer is thin, the excited waves can have very short wavelengths, the shortest ones being scaled by the intermediate region width. In other words, the characteristic spatial/time scale of the turbulence and the energy release fragmentation can be estimated by considering a typical width of the intermediate region where the turbulence originates. The width is determined basically by the angle between the RD and SMS, which is found to be, e.g., $\theta \approx 2^\circ$ at $M_{A00} = 0.1$ (Figure 2f, gray lines). At such an angle the width-to-length ratio of the intermediate region amounts to $\lambda/L \approx 1/30$. So, considering a range of reconnection rates, it can be concluded that the turbulence reduces the overall length-scale by 10–100 times. Taking for the overall current sheet length, scale $L = 10^4$–10^5 km, a typical reduced length-scale turns out to be in the range $\lambda = 100$–$10\,000$ km. Bearing in mind that the Alfvén velocity is of the order of 1000 km s^{-1}, one deduces that the turbulent regime is capable of creating fine structures on a wide range of time scales, from 0.1 to 10 s, such as required to explain the fragmentation of energy release in elementary flare bursts (De Jager, 1986).

In this respect, let us recall that the reconnection rate in the Petschek's regime depends on the magnetic Reynolds number as $M_{A00} \sim 1/\ln R_{\rm m}$ (cf., Priest, 1982 and references therein). Since the Reynolds number, $R_{\rm m} = Lv/\eta$, is inversely proportional to the resistivity η, it is important to take into account that in such small-scale current sheets the kinetic plasma instabilities are excited (e.g., Hoyng *et al.*, 1980; Spicer and Brown, 1981). The instabilities generate anomalous resistivity which can be more than 5 orders of magnitude larger (Kaplan and Tsytovich, 1973) than the classical one (Spitzer, 1962). Taking into account also the effect of the reduced length-scale (a factor of 10–100), one finds that the reconnection rate can be increased by a factor of 10–20, implying that the energy release can be locally strong.

Thus, the impulsive phase of two-ribbon flares, generally rich in fine structures, could be a consequence of the highly non-linear response of the system to small-amplitude fluctuations of the magnetic field direction around $\Omega_0 = 0$.

5.4. THE FLARE MORPHOLOGY

The most basic morphological change concerns the thermal/non-thermal character of flare. At higher reconnection rates (impulsive phase) the SMS loss-cone angle is larger (Figure 5), i.e., the magnetic mirrors at the SMSs are more open, and a larger number of energized electrons can escape from the outflow region along the field

lines. The downwards escaping electron beams excite reverse type III radio bursts, and cause strong electron precipitation at the foot-points, resulting in the non-thermal hard X-ray (HXR) emission there. Analogously, opening of the loss-cone in the outflow jet directed upwards from the diffusion region, provides for the escape of electron beams along the outward directed field lines (Figure 1-right), exciting metric-wavelength type III bursts. On the other hand, since the energy loss from the outflow region is large, the plasma above the flare loops does not attain temperatures which would provide the high-altitude HXR emission. Indeed, in the impulsive phase of the energy release, when the reconnection rate is high (as evidenced by fast expansion of ribbon fronts), the dominant features of the flare are non-thermal footpoint HXR sources accompanied by type III and reverse type III radio bursts.

When the reconnection rate becomes low (post-impulsive phase), the loss-cone angle at SMSs decreases from, say, 40 to 5°. That significantly reduces the number of escaping particles and the foot-point sources weaken. Similarly, the thermal conduction flux from the outflow region is reduced (e.g., Dowdy, Moore, and Wu, 1985) and the current sheet attains the highest temperature. Consequently, a hot source above the loop appears (Masuda *et al.*, 1994; Aschwanden *et al.*, 1996; Sui and Holman, 2003), presumably being located downstream of the FMS (see Section 5.1). If the FMS downstream plasma is dense enough, the source might even show characteristics of a thick-target HXR emission (Veronig and Brown, 2004).

Another intriguing morphological characteristic of the late phase of two-ribbon flares are "revivals" of type IV radio emission, usually showing up as several, successively weaker and smoother, post-maximum increases. Such an intermittent reawakening of electron acceleration during a predominantly thermal phase of the flare, might be related to an intermittent appearance of the turbulence which preferably happens at small Ω_0, below some critical value $\Omega_0^{\rm crit}$. It is reasonable to assume that due to the large-scale coronal inhomogeneities, the inflowing magnetic field shows variations in orientation of at least several degrees. So, the turbulence might be quenched in the periods with $\Omega_0 > \Omega_0^{\rm crit}$, and switched-on again when Ω_0 declines back to smaller values, $\Omega_0 < \Omega_0^{\rm crit}$. Since progressively larger scales are involved (overall current sheet stretching), the spatial and time scales involved become larger, and fine structures become blurred.

Gradually, the energy release diminishes due to increasing β_0 in the ambient plasma, and eventually the flare ceases. However, the reconnection can still be going on long after the flare ends, as evidenced by a continuing growth of colder, "post-eruption" loops.

Appendix A: Solutions of the Complete $2\frac{1}{2}$-D Problem

The coupled system of jump relations at SMS and RD was transformed by Skender, Vršnak, and Martinis (2003) into 17 equations containing 21 dimensionless quantities. There are several possible choices of four input parameters that provide

solutions in an explicit form. Unfortunately, that does not include the case where the outflow and intermediate region parameters are presented as explicit functions of the four inflow region parameters (Ω_0, β_0, M_{A00}, and α). So, the problem has to be inverted: we have to chose one of the explicit-solution options, and then the four chosen variables have to be varied iteratively until the desired values of Ω_0, β_0, M_{A00}, and α are achieved. It turns out that most convenient option is to employ as variables the density jump $N_{12} = n_2/n_1 \equiv N$ and the angles δ, ε, and ξ' (see Figure 1-left for definitions of the angles used here and later).

In the following we present explicit expressions for all relevant quantities, in the form of an algorithm that can be straightforwardly employed for a numerical evaluation, and this is what we have used to obtain the results presented in this paper. The ratio of specific heats is assumed to be 5/3.

Starting with the input values of N, δ, ε, and ξ', first we find the angles γ and ϕ:

$$\gamma = \varepsilon - \delta, \tag{A.1}$$

$$\phi = \frac{1}{2}\arcsin\frac{2\sin\varepsilon\sin\delta}{N\sin\gamma}, \tag{A.2}$$

and the following three SMS-related parameters:

$$V_r \equiv \frac{v_{r2}}{v_{r1}} = \frac{\cos\phi\sin\gamma}{\sin\delta}, \tag{A.3}$$

$$B_r \equiv \frac{B_{r2}}{B_{r1}} = \frac{\sin\delta}{\cos\phi}, \tag{A.4}$$

$$M_{A1r} \equiv \frac{v_{r1}\sqrt{\mu\rho_1}}{B_{r1}} = \sqrt{\frac{\sin\delta\cos\delta - B_r^2\sin\phi\cos\phi}{\sin\varepsilon\cos\varepsilon + NV_r^2\sin\phi\cos\phi}}. \tag{A.5}$$

Here, μ denotes the permeability and ρ is the plasma density. Now, the rest of relevant xy-plane angles can be evaluated:

$$\phi' = \arctan\frac{\sin\gamma}{M_{A1r} - \cos\gamma}, \tag{A.6}$$

$$\omega = \pi - \phi' - \gamma, \tag{A.7}$$

$$\theta = \delta - \omega, \tag{A.8}$$

$$\alpha = (\pi - \xi') + \phi + \vartheta, \tag{A.9}$$

$$\delta' = \arctan\frac{1}{\cot\omega + \cot\phi' - \cot\xi'}, \tag{A.10}$$

$$\sigma = \theta + \phi - \delta'. \tag{A.11}$$

After calculating two RD-related parameters,

$$B_r' \equiv \frac{B_{r1}}{B_{r0}} = \frac{\sin\delta'}{\sin\omega}, \tag{A.12}$$

$$V_r' \equiv \frac{v_{r1}}{v_{r0}} = \frac{\sin\xi'}{\sin\phi'}, \tag{A.13}$$

the direction of the intermediate region flow can be determined:

$$\Omega_V = \arctan\sqrt{\frac{H^2-1}{D^2-G^2H^2}}, \tag{A.14}$$

where

$$H = \frac{\sin\omega}{\sin\delta'}, \tag{A.15}$$

$$D = M_{A1r}^2\frac{\sin\varepsilon}{\sin\delta} + \frac{B_r\cos\phi\left(\sin\delta - M_{A1r}^2\frac{\sin^2\varepsilon}{\sin\delta}\right)}{B_r\sin\varepsilon\cos\phi - V_r\sin\phi\sin\delta}, \tag{A.16}$$

$$G = D\frac{B_r'^2\sin\omega}{\sin\delta'} + \frac{V_r'^2\sin\phi'\left(B_r'^2\sin\omega\cos\omega - \sin\delta'\cos\delta'\right)}{\sin\delta'\left(\sin\xi'\cos\xi' - V_r'^2\sin\phi'\cos\phi'\right)}. \tag{A.17}$$

The expressions for the inclination of the magnetic field in the inflow, intermediate, and outflow region read

$$\Omega_0 = \arctan\left(G\tan\Omega_V\right), \tag{A.18}$$

$$\Omega_1 = \arctan\left(D\tan\Omega_V\right), \tag{A.19}$$

$$\Omega_2 = \arctan\frac{\tan\Omega_1\sin\varepsilon - \tan\Omega_V\sin\delta}{V_rB_r\sin\phi}, \tag{A.20}$$

respectively.

The pressure jump at the SMS amounts to

$$P \equiv \frac{p_2}{p_1} = \frac{\frac{4F}{5E} + \sin\varepsilon}{V_r\sin\phi + \frac{4F}{5E}}, \tag{A.21}$$

where

$$E = 2M_{A1r}^2\left(\sin^2\varepsilon - NV_r^2\sin^2\phi\right) + \frac{1}{\cos^2\Omega_1} - \frac{B_r^2}{\cos^2\Omega_2}, \tag{A.22}$$

$$F = F_1 + F_2 + F_3, \tag{A.23}$$

$$F_1 = -\frac{1}{2}M_{A1r}^2\left(\frac{\sin\varepsilon}{\cos^2\Omega_V} - NV_r^3\sin\phi\right) - \tan^2\Omega_1\sin\varepsilon, \tag{A.24}$$

$$F_2 = B_r^2V_r\tan^2\Omega_2\sin\phi - \cos^2\delta\sin\varepsilon + B_r^2V_r\sin^3\phi, \tag{A.25}$$

$$F_3 = \sin\delta\tan\Omega_1\tan\Omega_V + \sin\delta\cos\delta\cos\varepsilon + B_r^2V_r\sin\phi\cos^2\phi. \tag{A.26}$$

The physical state of the output is completed by evaluating the temperature jump at the SMS,

$$\frac{T_2}{T_1} \equiv T = \frac{P}{N}, \tag{A.27}$$

and the magnetosonic Mach number of the outflow:

$$M_2 \equiv \frac{v_2}{\sqrt{\frac{B_2^2}{\mu\rho_2} + \frac{5\rho_2}{3\rho_2}}} = \frac{V_r M_{A1r}\sqrt{N}}{\sqrt{\frac{B_r^2}{\cos^2\Omega_2} + \frac{5P\beta_0}{6\cos^2\Omega_1}}}. \tag{A.28}$$

Finally, the plasma-to-magnetic pressure ratio in the inflow region, and the reconnection rate can be obtained from

$$\beta_0 = \beta_1 = \frac{E}{P-1}\cos^2\Omega_1 \tag{A.29}$$

and

$$M_{A00} = \frac{\sin\alpha\sin\delta'}{\sin(\pi - \xi')\cos(\delta' + \vartheta + \phi)}, \tag{A.30}$$

respectively.

Appendix B: Soward's Approximation

Soward's approximation (Soward, 1982) is sufficiently good to describe the behaviour of the temperature, density, and magnetic field strength for the $\alpha = 90^\circ$ case. Since the outcome is relatively simple, it is possible to represent it in a compact, ready-to-use form. In order to avoid duplication of the symbols, the parameters denoted in the original paper as α and δ, we rename herein to a and d, respectively. The parameter $a \equiv n_1/n_2$ represents the inverse of the density jump, $a \equiv 1/N$.

Neglecting small terms in the jump relations at the RD and the SMS, the system of equations decouples into two partly independent subsets. The first subset relates the inflow and outflow quantities and does not depend on the reconnection rate M_{A00}. The density ratio a can be expressed explicitly in terms of the transversal magnetic field jump at the SMS, $q = B_{z2}/B_{z1}$:

$$a = \frac{5\beta_0 + 2 - 2q}{5\beta_0 + 5 - 2q - 3q^2}, \tag{B.1}$$

where we have taken the ratio of specific heats to be $5/3$. Introducing the parameter d,

$$d = \left(\frac{1-q}{1-aq}\right)^{1/2}, \tag{B.2}$$

the angle Ω_0 can be expressed as

$$\sin \Omega_0 = \frac{q(1+ad)}{1+d}, \tag{B.3}$$

whereas β_2 reads

$$\beta_2 = \frac{\beta_0 + 1 - q^2}{q^2}. \tag{B.4}$$

Finally, the temperature jump is

$$\frac{T_2}{T_1} = \frac{T_2}{T_0} = \frac{\beta_2}{\beta_0} a q^2, \tag{B.5}$$

and the density ratio is by definition

$$\frac{n_2}{n_1} = \frac{n_2}{n_0} = \frac{1}{a}. \tag{B.6}$$

Note that for a given value of β_0, the parameters q and a cannot be expressed as explicit functions of Ω_0. So, the system has to be solved iteratively (varying q, until Ω_0 becomes adjusted to the prescribed value). Finally note, that for $\beta_0 \ll 1$ and $\Omega_0 \approx 0$, the pressure ratio behaves as $p_2/p_1 = TN = T/a \approx 1/\beta_0$.

The other subset of equations determines the behaviour of the angles ϕ, θ, δ', and σ (see Figure 1), which depend also on M_{A00}. They can be expressed (in radians) as

$$\delta' = M_{A00}, \tag{B.7}$$

$$\phi = ad\, M_{A00}, \tag{B.8}$$

$$\sigma = (2 + ad - d) M_{A00}, \tag{B.9}$$

and

$$\theta = \sigma - \phi - \delta'. \tag{B.10}$$

All the angles are proportional to M_{A00}, i.e., they increase with an increasing reconnection rate.

References

Antiochos, S. K., DeVore, C. R., and Klimchuk, J. A.: 1999, *Astrophys. J.* **510**, 485.
Aschwanden, M. J.: 2002, *Space Sci. Rev.* **101**, 1.
Aschwanden, M. J., Hudson, H. S., Kosugi, T., and Schwartz, R. A.: 1996, *Astrophys. J.* **464**, 985.
Aurass, H.: 2004, in T. Sakurai and T. Sekii (eds.), *Solar-B Mission and the Forefront of Solar Physics*, ASP Conference Series, Vol. 325, in press.
Aurass, H., Vršnak, B., and Mann, G.: 2002, *Astron. Astrophys.* **384**, 273.
Aurass, H., Vršnak, B., Hofmann, A., and Ruždjak, V.: 1999, *Solar Phys.* **190**, 267.

Brown, M. R., Cothran, C. D., Landerman, M., Schlossberg, D., and Matthaeus, W. H.: 2002, *Astrophys. J.* **577**, L63.
Bulanov, S. V., Dogel, V. A., and Frank, A. G.: 1984, *Sov. Astron Lett.* **19**, 59.
Cargill, P. J. and Priest, E. R.: 1982, *Solar Phys.* **76**, 357.
Cargill, P. J., Chen, J., Spicer, D. S., and Zalesak, S. T.: 1996, *J. Geophys. Res.* **101**, 4855.
Chen, P. F., Shibata, K., Brooks, D. H., and Isobe, H.: 2004, *Astrophys. J.* **602**, L61.
Cheng, C. Z., Ren, Y., Choe, G. S., and Moon, Y.-J.: 2003, *Astrophys. J.* **596**, 1341.
Craig, I. J. D. and Litvinenko, Yu. E.: 2002, *Astrophys. J.* **570**, 387.
De Jager, C.: 1986, *Space Sci. Rev.* **44**, 43.
Dmitruk, P., Matthaeus, W. H., Seenu, N., and Brown, M. R.: 2003, *Astrophys. J.* **597**, L81.
Dowdy, J. F. Jr., Moore, R. L., and Wu, S. T.: 1985, *Solar Phys.* **99**, 79.
Feldman, W. C., Schwartz, S. J., Bame, S. J., *et al.*: 1984, *Geophys. Res. Lett.* **11**, 599.
Feldman, W. C., Baker, D. N., Birn, J., *et al.*: 1985, *J. Geophys. Res.* **90**, 233.
Feynman, J. and Ruzmaikin, A.: 2004, *Solar Phys.* **219**, 301.
Forbes, T. G.: 1986, *Astrophys. J.* **305**, 553.
Forbes, T. G. and Acton, L. W.: 1996, *Astrophys. J.* **459**, 330.
Forbes, T. G. and Malherbe, J. M.: 1986, *Astrophys. J.* **302**, L67.
Forbes, T. G. and Malherbe, J. M.: 1991, *Solar Phys.* **135**, 361.
Forbes, T. G. and Priest, E. R.: 1983, *Solar Phys.* **84**, 169.
Frank, A. G., Bogdanov, S. Yu., and Markov, V. S.: 2002, in A. Wilson (ed.), *Solar Variability: From Core to Outer Frontiers*, ESA SP-506, p. 609.
Furth, H. P., Kileen, J., and Rosenbluth, M. N.: 1963, *Phys. Fluids* **6**, 459.
Gary, G. A.: 2001, *Solar Phys.* **203**, 71.
Gekelman, W. and Pfister, H.: 1988, *Phys. Fluids* **26**, 1949.
Heitsch, F. and Zweibel, E. G.: 2003, *Astrophys. J.* **590**, 291.
Hoyng, P., Duijveman, A., van Grunsven, T. F. J., and Nicholson, D. R.: 1980, *Astron. Astrophys.* **91**, 17.
Innes, D. E., McKenzie, D. E., and Wang, T.: 2001, *Solar Phys.* **217**, 267.
Irby, J. H., Drake, J. F., and Griem, H. R.: 1979, *Phys. Rev. Lett.* **42**, 228.
Isliker, H., Anastasiadis, A., and Vlahos, L.: 2001, *Astron. Astrophys.* **377**, 1068.
Kahler, S. W., Moore, R. L., Cane, S. R., and Zirin, H.: 1988, *Astrophys. J.* **328**, 824.
Kaplan, S. A. and Tsytovich, V. N.: 1973, *Plasma Astrophysics*, Pergamon Press, Oxford.
Kundu, M. R., Garaimov, V. I., White, S. M., and Krucker, S.: 2004, *Astrophys. J.* **600**, 1052.
Lin, J.: 2004, *Solar Phys.* **219**, 169.
Lin, J. and Forbes, T. G.: 2000, *J. Geophys. Res.* **105**, 2375.
Litvinenko, Yu. E.: 2003, *Solar Phys.* **212**, 379.
Litvinenko, Yu. E. and Somov, B. V.: 1993, *Solar Phys.* **146**, 127.
Low, B. C.: 2001, *J. Geophys. Res.* **106**, 25141.
Magara, T., Mineshige, S., Yokoyama, T., and Shibata, K.: 1996, *Astrophys. J.* **466**, 1054.
Martens, P. C. H. and Kuin, N. P. M.: 1989, *Solar Phys.* **122**, 263.
Masuda, S., Kosugi, T., Hara, H., Tsuneta, S., and Ogawa, Y.: 1994, *Nature* **371**, 495.
McKenzie, D. E.: 2000, *Solar Phys.* **195**, 381.
McKenzie, D. E. and Hudson, H. S.: 1999, *Astrophys. J.* **519**, L93.
Nishikawa, K.-I. and Sakai, J.: 1982, *Phys. Fluids* **25**, 1384.
Petrosian, V., Donaghy, T. Q., and McTiernan, J. M.: 2002, *Astrophys. J.* **569**, 459.
Petschek, H. E.: 1964, in W. N. Hess (ed.), *AAS-NASA Symposium on Physics of Solar Flares*, NASA SP-50, p. 425.
Petschek, H. E. and Thorne, R. M.: 1967, *Astrophys. J.* **147**, 1157.
Priest, E. R.: 1982, *Solar Magnetohydrodynamics*, Reidel, Dordrecht.
Saito, K.: 1970, *Ann. Tokyo Astr. Obs.* **12**, 53.

Sakurai, T.: 1993, *Adv. Space Res.* **13**, 109.
Sato, T. and Hayashi, T.: 1979, *Phys. Fluids* **22**, 1189.
Shay, M. A., Drake, J. F., Denton, R. E., and Biskamp, D.: 1998, *J. Geophys. Res.* **103**, 9165.
Shay, M. A., Drake, J. F., Rogers, B. N., and Denton, R. E.: 2001, *J. Geophys. Res.* **106**, 3759.
Skender, M., Vršnak, B., and Martinis, M.: 2003, *Phys. Rev. E* **68**, 0464XX.
Smith, E. J., Slavin, J. A., Tsurutani, B. T., Feldman, W. C., and Bame, S. J.: 1984, *Geophys. Res. Lett.* **11**, 1054.
Somov, B. V.: 1986, *Astron. Astrophys.* **163**, 210.
Somov, B. V. and Kosugi, T.: 1997, *Astrophys. J.* **485**, 859.
Somov, B. V. and Titov, V. S.: 1985, *Solar Phys.* **102**, 79.
Soward, A. M.: 1982, *J. Plasma Phys.* **28**, 415.
Spicer, D. S. and Brown, J. C.: 1981, in S. Jordan (ed.), *The Sun as a Star*, NASA SP-450, Washington, p. 413.
Spitzer, L.: 1962, *Physics of Fully Ionized Gasses*, Intersciece, New York.
Stenzel, R. L. and Gekelman, W.: 1979, *Phys. Rev. Lett.* **42**, 1055.
Sui, L. and Holman, G. D.: 2003, *Astrophys. J.* **596**, L251.
Švestka, Z.: 1976, *Solar Flares*, Reidel, Dordrecht.
Tsuneta, S.: 1996, *Astrophys. J.* **456**, 840.
Tsuneta, S. and Naito, T.: 1998, *Astrophys. J.* **495**, L67.
Uchida, Y., Wheatland, M. S., Haga, R., Yoshitake, I., and Melrose, D.: 2001, *Solar Phys.* **202**, 117.
Ugai, M.: 1987, *Geophys. Res. Lett.* **14**, 103.
Ugai, M.: 1992, *Phys. Fluids B* **4**, 2953.
Veronig, A. and Brown, J. C.: 2004, *Astrophys. J.* **603**, L117.
Vršnak, B.: 1989, *Solar Phys.* **120**, 79.
Vršnak, B.: 2003, in K.-L. Klein (ed.), *Energy Conversion and Particle Acceleration in the Solar Corona*, Lecture Notes on Physics, Springer, Heidelberg, vol. 612, p. 28.
Vršnak, B.: 2004, in A. Hanslmeier, A. Veronig, and M. Messerotti (eds.), *Solar Magnetic Phenomena*, Kluwer Academic Publishers, Dordrecht, p. 27.
Vršnak, B. and Lulić, S.: 2000, *Solar Phys.* **196**, 157.
Vršnak, B., Magdalenić, J., Aurass, H., and Mann, G.: 2002, *Astron. Astrophys.* **396**, 673.
Vršnak, B., Klein, K.-L., Warmuth, A., Otruba, W., and Skender, M.: 2003, *Solar Phys.* **214**, 325.
Wang, H., Qiu, J., Ju, J., and Zhang, H.: 2003, *Astrophys. J.* **593**, 564.
Withbroe, G. L.: 1988, *Astrophys. J.* **325**, 442.
Wu, S. T., Zheng, H., Wang, S., Thompson, B. J., Plunkett, S. P., Zhao, X. P., and Dryer, M.: 2001, *J. Geophys. Res.* **106**, 25089.
Yokoyama, T. and Shibata, K.: 1997, *Astrophys. J.* **474**, L61.
Yokoyama, T. and Shibata, K.: 2001, *Astrophys. J.* **549**, 1160.
Yokoyama, T., Akita, K., Morimoto, T., Inoue, K., and Newmark, J.: 2001, *Astrophys. J.* **546**, L69.